

# A Characterization of the Initiation of the Summer Diurnal Evolution Convection in the Catalan Pyrenees: an 11-year (2010-2020) Radar-Data Based Analysis

F. Vilar-Bonet<sup>1</sup> and T. Rigo<sup>2</sup>

<sup>1</sup>Landscape Survey (SGEP), University of Barcelona.

<sup>2</sup>Servei Meteorològic de Catalunya.

Received: 3-XI-2021 – Accepted: 28-IV-2022 – **Original version**

Correspondence to: fvilar@ub.edu

## Abstract

*The Radar Network of the Meteorological Service of Catalonia provides volumetric coverage of the entire region of Catalonia. With respect to the Pyrenees, this network allows us to identify the complete life cycle of thunderstorms accurately, despite low level beam-blockage caused by topography. This research paper focuses on convection initiation, and considers that only those cases of diurnal evolution selected, and the first daily thunderstorm. The spatial distribution of the first daily convective echoed in the Western and Eastern Catalan Pyrenees reveals obvious differences, with a predominance of the second sector. Furthermore, as the reflectivity threshold used increases, the differences between both areas also rise. The selected discriminating reflectivity values used in the analysis were 15, 35 and 45 dBZ, and correspond to weak, moderate, and heavy precipitation. However, this difference arises from the influence of the county of El Ripollès, where over 30% of the initial convection for all three reflectivity thresholds occurs. Finally, a high spatial resolution analysis has allowed us to detect how the northern part of the abovementioned county is the most relevant hotspot in terms of initial convection in the Catalan Pyrenees.*

**Key words:** diurnal evolution convection, radar reflectivity, Catalan Pyrenees, spatial analysis, time analysis, topography

## 1 Introduction

The Pyrenees is an area commonly-affected by heavy rainfall that often produces severe floods that damage the infrastructure and cause casualties, many examples of which are summarized in Pino et al. (2016). The PIRAGUA project is responsible for providing a database that covers the entire Pyrenean region (Aznárez-Balta et al., 2020). The most noteworthy cases are those of November 1982 (Llasat and Puigcerver, 1994) or June 2013 (Corripio and López-Moreno, 2017), in the Catalan Pyrenees, and that of August 1996 (Riosalido et al., 1997) in the Central Pyrenees, which caused 96 casualties and heavy damages to a camping site. Applying a locally-based focus, Abancó et al. (2016) analysed the avenues in a small basin of the Western Catalan Pyrenees, showing how weather radar helps to improve the accuracy of rainfall fields, rather than using rain gauge data alone.

The climate of Catalan Pyrenees and Pre-Pyrenees depends on different factors. The main factor being the disposition and distribution of the valleys and mountain ranges. Other aspects include the altitude, the topography and the area's proximity to the Mediterranean Sea. Most of the region pertains to the Mediterranean climatic region. However some differential features are involved that concern the habitual Mediterranean climate. One of the main unique features is that, although the Mediterranean basin is generally characterized by the fact that the summer is the driest season of the year (Jansa et al., 2017), in most of the Catalan Pyrenean area, the opposite occurs, meaning that summer is the rainiest season - with the exception of the two extremes, the western and the eastern regions (Meteorological Service of Catalonia, 2008).

Current research on convection analysis using weather radar provides numerous contributions. Most of these studies rely on 3D identification and the tracking of convective

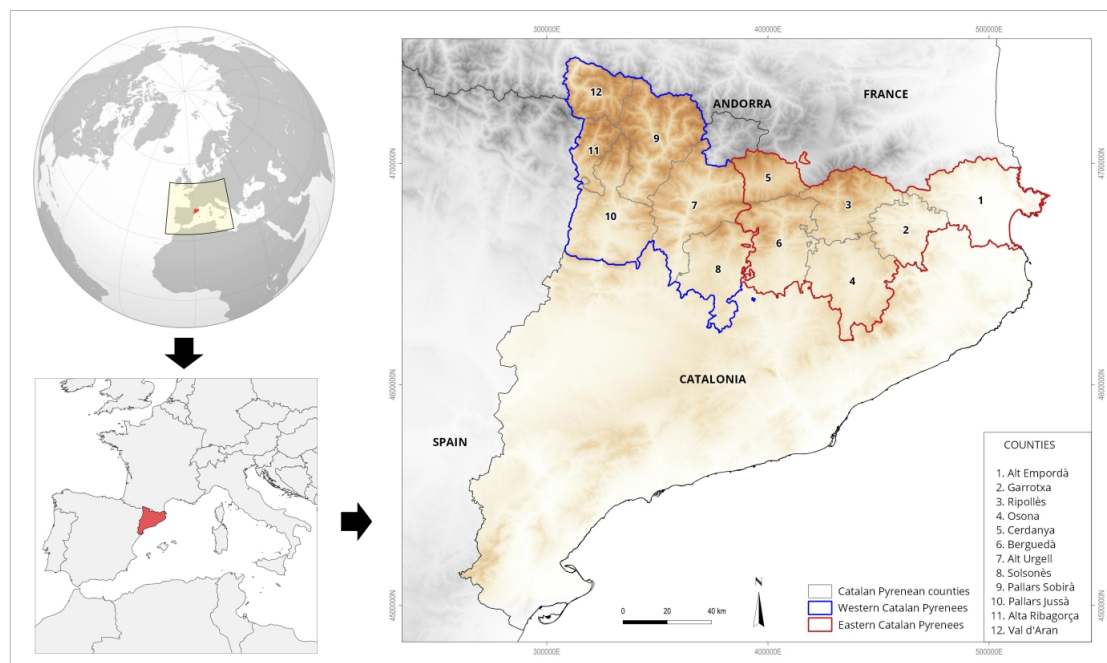


**Figure 1:** Global map with the Southwestern European region marked in yellow (top left). Southwestern European region with Catalonia highlighted in red (bottom left) and a map of Catalonia with the selected counties in the study. Blue line delimits the Western Pyrenees area, while a red line marks the limits of the Eastern Pyrenees region (right).

cells, along with their life cycle and trajectory (Utsav et al., 2017; Goudenhoofd and Delobbe, 2013; del Moral et al., 2018; Frye and Mote, 2010; Mecikalski et al., 2008; Rigo and Llasat, 2016; Rigo et al., 2010). However we have only encountered one specific investigative work that systematically refers to initial convection (Bai et al., 2020), which presented a methodology for identifying initial convection in the coastal area of China. The analysis included two thresholds: one of 10 dBZ for estimating minimum rainfall and, on the other hand, a combination of 35 and 40 dBZ with respect to the identification of the convective part. These thresholds are like those used in the other cited works. The extreme value was 45 dBZ for convection identification. The main issue found by Bai et al. (2020) corresponded to those errors in radar imagery, which hindered the application of the technique in an automatic mode. In this case, topographic blockage resulted in the underestimation of radar beam data in some regions.

Moving on to the convection initiation linked to the topographic factor, Weckwerth and Parsons (2006) considered orography to be one of the main elements responsible for triggering thunderstorms linked to dry lines, frontal lines or wind gusts, among others. They presented examples of how convection develops in a well-organized mode, even on days of synoptic stability. Similar characteristics had previously been found by Wilson et al. (1988). Both studies belonged to different projects that focused on the observational analysis of convection in the Great Plains of North America. Huang et al. (2017) in China and Aoshima et al. (2008) in Germany observed that convection initiation revealed positive correlation with the diurnal convection cycle through the use of satellite data. The

maximum activity was around 13 UTC in the first case and 13 LST (UTC + 8 hours) in the second. Furthermore, the first analysis showed the highest activity levels during the summer season.

With respect to Catalonia and the Pyrenees in particular, only a few references to convection initiation exist. Probably, the most relevant analysis is that of Pascual et al. (2004), which includes the relative frequency of 35 dBZ radar echoes at 15.00 UTC during the summer months of 2003. They observed topographic influence on the map. Pineda et al. (2011) showed that thunderstorm days in the counties of the Pyrenees counties oscillated between 26 and 39 from 2004 to 2008. They also found two maxima, one in the western part of the area and the other in the central region. In both cases, the number of those days when thunderstorms occurred exceeded a value of 30. Furthermore, the number of stormy days decreases as we move to the plains and coastal areas. The map changes notably in terms of lightning density, with a hotspot of 4 flashes per square kilometre in the central region. Finally, the study concludes with the maximum lightning activity in the Pyrenees during the summer months. del Moral et al. (2017) detected a maximum number of thunderstorms in the Central Pyrenees from 2008 to 2015. The analysis led to the development and application of an algorithm for the identification of convective cells using weather radar. Part of the methodology considered in this study has served as a reference for this investigation. Farnell and Rigo (2020) showed that the number of *Lightning Jump* warnings also registered maximum figures over the same region between 2006 and 2018. These warnings closely coincide with severe weather occurrences (large hail, tornadoes, and convective

**Table 1:** A List of Counties in Both Sectors (Eastern and Western Pyrenees) and their Surface Area.

Sector	County	Surface (km <sup>2</sup> )
Eastern Pyrenees	1 Alt Empordà	1,357.5
	2 Garrotxa	734.6
	3 Ripollès	956.6
	4 Osona	1,245.2
	5 Cerdanya	546.7
	6 Berguedà	1,185.3
Western Pyrenees	7 Alt Urgell	1,447.5
	8 Solsonès	1,001.2
	9 Pallars Sobirà	1,377.9
	10 Pallars Jussà	1,343.1
	11 Alta Ribagorça	426.9
	12 Val d'Aran	633.6

winds). Finally, Conde Iglesias (2021) identified different thunderstorms nests using the Meteorological Service of Catalonia lightning location system for the months April to September during the period 2016 to 2020. The author considered the first five intra-cloud flash position in a field with a 20x20 km<sup>2</sup> spatial resolution. The main result was the identification of thunderstorm nests that related to the topography. The main aim of this work is to characterize the initiation of diurnal evolution convection during the summer period in the Catalan Pyrenees from a time and spatial standpoint. This analysis has took eleven years of radar imagery into account. The paper includes the following sections. It firstly presents the study area and the data used; the following sections refer to the methodology and the results obtained, before finally detailing the conclusions reached.

## 2 Study and Data Area

### 2.1 Area and Analysis Period

The area of study comprised the Catalan Pyrenees and Pre-Pyrenees (Fig. 1). County limits have been used to simplify the geographical analysis. The selection includes all those counties covered, either totally or partially, by one or both mountain ranges. Twelve counties meet these criteria. The surface area of these counties varies greatly (Table 1), and ranges between 1,447.5 km<sup>2</sup> (L'Alt Urgell being the largest) and 426.9 km<sup>2</sup> (L'Alta Ribagorça being the smallest). This point is significant when analysing spatial influence in each county. The total area has also been divided into two sectors: the Western and the Eastern Pyrenees/Pre-Pyrenees. These two blocks are highly homogeneous in terms of the number of counties (6 in each) and their total surface area: 6,025.9 km<sup>2</sup> in the eastern sector and 6,230.2 km<sup>2</sup> in the western part (Fig. 1 and Table 1).

With respect to the period of analysis, this study focuses on the summer months (June, July, and August), from 2010 to 2020. Several studies (e.g. Núñez et al. (2018)) showed that diurnal convection mainly occurs during these months.

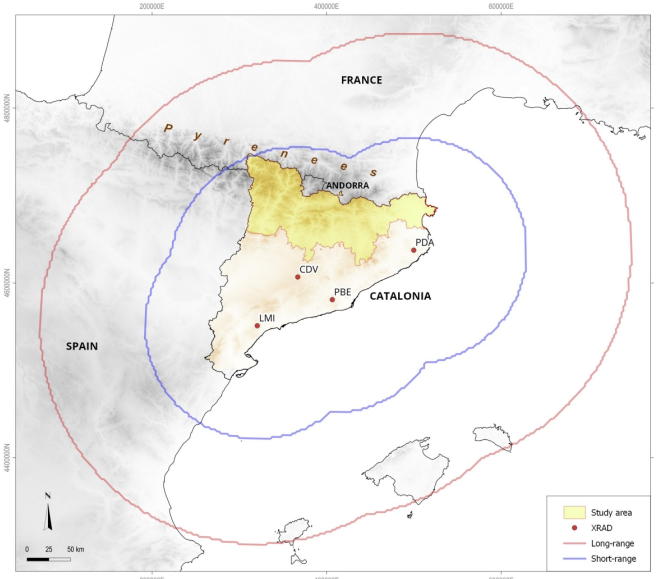


**Figure 2:** The location of the four radars in the XRAD Radar Network (XRAD) Meteorological Service of Catalonia. The yellow shaded area corresponds to the study region (see Fig. 1). The red and blue lines indicate the range of the two radar modes: surveillance (long) and volumetric (short).

These authors also noted that convection is equally prevalent during periods in May and September. However these two months have not been selected in this analysis due to irregularities in their occurrence.

### 2.2 The Data Used

The data used in the analysis was radar imagery from the Meteorological Service of Catalonia (SMC). The imagery consists of composites from the long-range data of the four radar stations (Fig. 2) in the SMC network (XRAD): the radar of La Panadella-Creu del Vent (CDV), Vallirana-Puig Bernat (PBE), Cruïlles-Puig d'Arques (PDA) and Tivissa-La Miranda (LMI). The four radars cover the entire area of Catalonia in both short-range mode (130 or 150 km, depending on the radar) and long-range mode (250 km). Both forms have a spatial resolution of 1 km and a time resolution of 6 minutes, which is the resolution of the composite product used in the study.

The products used in this analysis were: daily quantitative precipitation estimation (QPE) and Constant Altitude Plan Position Indicator (CAPPI) at 1 km. With respect to the first product, the daily QPE is an accumulated rainfall estimation for the entire Catalan region that combines corrected radar data and the automatic weather station data of the SMC. Rigo et al. (2021) provide detailed information on this product with respect to the data generation process and its advantages and limitations. CAPPI 1 km shows the location and intensity of the echoes at a theoretical and constant height, at one kilometre above sea level. The SMC generates this product using the interpolation of those points close to this altitude for distinct elevations. The

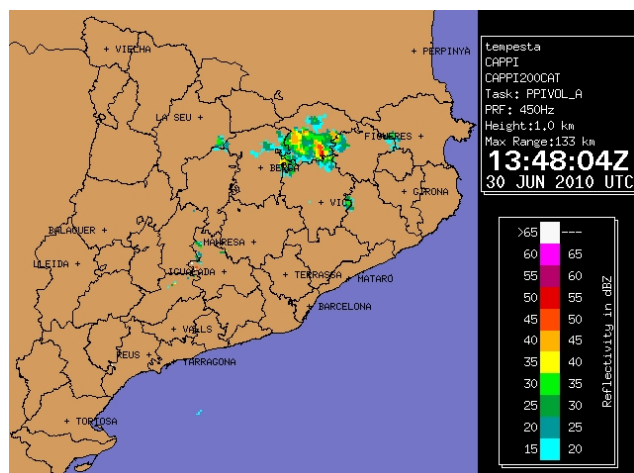


**Figure 3:** An example of a planar GIF radar image for manual classification. (Source: Meteorological Service of Catalonia).

composite product combines the data from the four radars, using the maximum value at each pixel of 1km resolution. This study has considered planar imagery in GIF (Fig. 3) and georeferenced GeoTIFF imagery formats. The GeoTIFF format allows data to be mathematically processed using programs such as R (R Core Team, 2013) and QGIS (Gray, 2008).

The main limitations of the CAPPI 1 km imagery that affected the analysis are detailed below: (the Meteorological Service of Catalonia, 2013 provides more information):

- **Topographic blockage:** the lowest beam of the closest radars to the analysis region is either partially or totally blocked in some azimuths. Using a composite product reduces this issue (CDV -blockage between 50 and 90% in the Central part-, PBE -close to 70% in the county of l'Alt Urgell- and PDA -about 75% in the Eastern Pyrenees-). However, there are some cases in which part of the echo structure is mismatched. This phenomenon occurs mainly in the case of a lower reflectivity threshold, and this may also happen in some parts of the life cycle of the convective cell. The vertical development of the thunderstorms renders the limitation lower than in the case of winter episodes. In this case the product observes, at least, a portion of the cell, although some echoes are mismatched. The spotters in the studied area confirmed in several episodes that the trajectory of the majority of thunderstorms agreed with the visual identification.
- **Beam height:** this issue has a close relationship with that mentioned above. Each radar station covers the analysed area at a different altitude (CDV between 1.5 and 4 km, PBE 2 to 6 km, LMI between 3 and 7 km, or PDA 0.5 to 5.5 km). This fact means that each radar would perceive a determined thunderstorm in a different manner.

- **Electromagnetic interferences (EMI):** the well-known pattern consists of a linear structure that departs from a radar location and low to moderate reflectivity values (Altube et al., 2015). The issue is that the pattern does not remain constant over time. The application of an automatic method for removing EMI is complicated. All XRAD radar suffer from these anomalies, however the most evident anomaly affected CDV radar during some summer months during the period of investigation and this will be the one referred to in the following sections. These interferences do not present problems in convection identification at elevated thresholds (35 and 45 dBZ), however they do cause problems at a lower limit (15 dBZ).
- **Lack of one or more radars in the compound:** although the XRAD radars have a robust behaviour in general, there were different, short periods in which one (or more) of them was unable to contribute to the final product used. During the study period the PBE (2013-2016) and LMI (2020) radar stations did not contribute, as their systems were undergoing renovation. Several radar shutdowns also took place (due to maintenance or communication problems in episodes of heavy rain). Several experiments that were made on those days when all the available radars allowed the influence of the lack of one or more radars to be determined. Generating compounds without one or more radars helped to ensure that the area of interest was always well-identified. Furthermore, the variations in the surface only reached, at most, 12% of the total.

The manual use of GIF images has allowed us to minimize the impact of the previously-mentioned problems. The detection of the anomalies led us to process the GeoTIFF files using an automatic method.

### 3 Methodology

As shown above, the establishment of a methodology for the classification of convective structures is quite complex. This fact is due to the multitude of criteria to be defined and applied (Rigo and Llasat, 2004). In our case, it was first necessary to preselect the candidate days that met the imposed conditions a priori. The images were then analysed in detail -according to the established criteria- and rejected or accepted. In the second case, they can be classified by influence in accordance with region, time, and the previously-established reflectivity threshold. Fig. 4 summarizes the classification workflow used in this research, which will be explained below.

#### 3.1 The Selection of Candidate Days

The total number of days to for analysis comes to 1,012, corresponding to the summer seasons of the 11 years



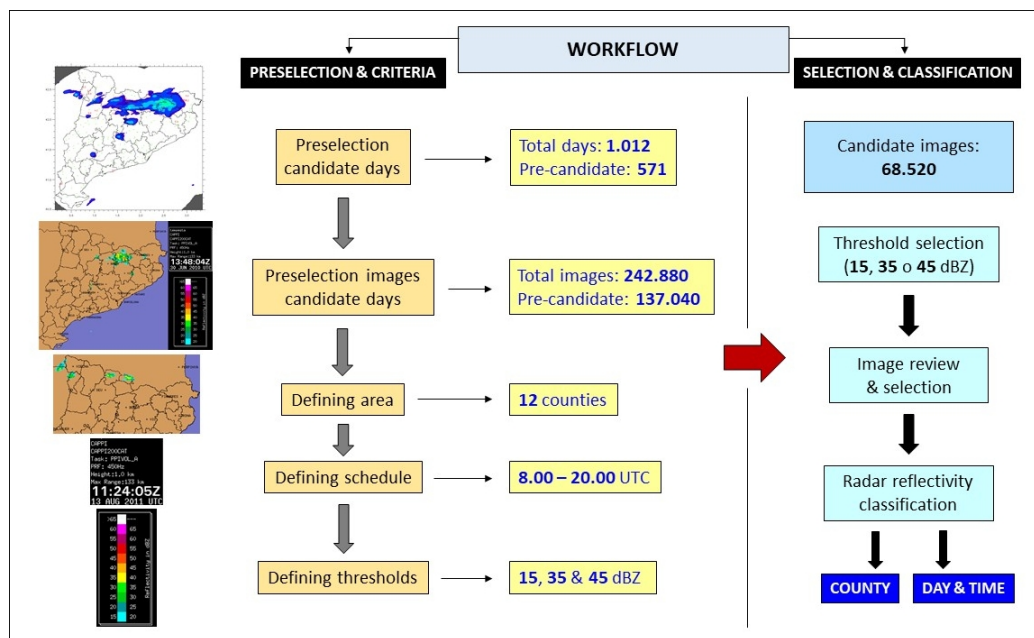


**Figure 4:** The workflow scheme of the methodology for identifying and classifying convection initiation echoes of 15, 35 and 45 dBZ.

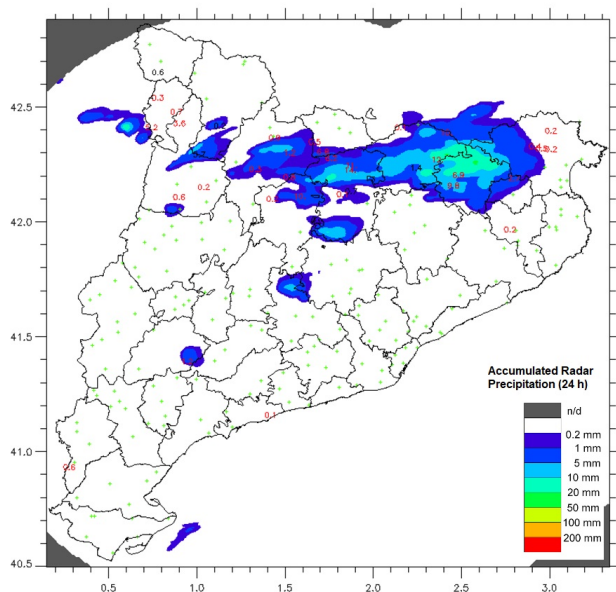


**Figure 5:** An example of the daily precipitation estimation field (18 August, 2010), combining corrected radar estimation with automatic weather station registers (Source: Meteorological Service of Catalonia).

covered by the study period: 2010-2020. Given that the images are of a six-minute frequency, this task involved reviewing a very high number of images (242,800). A previous analysis was therefore conducted to reduce the selection of those candidate days to be studied. This work involved the daily imagery of the accumulated precipitation fields, and combined radar data and automatic weather stations (see an example in Fig. 5). In brief, we managed to make a preliminary selection, which included 571 days and a

reduction of the total number of candidate images to 137,040.

## 3.2 The Definition of Criteria

### 3.2.1 The Diurnal Evolution Period

Precipitation originates from different causes. Rising air responds to four main mechanisms: convective, frontal, orographic and ascent by convergence, which all lead to different types of precipitation. This paper focuses on convective echoes deriving from diurnal evolution, that is those caused by the direct heating of the air through radiation. The echoes or convective precipitation analysed does not therefore allude to the intensity of rainfall –and classifies precipitation as lying between convective and stratiform–however its cause is referred to.

Assigning a cause in the appearance of echoes is quite a complex task, as it is not often the result of a single cause, but rather the consequence of a combination of the latter. There may be a convective factor, a convergence, or an orographic factor, among others. In all events, the classification has been made while placing emphasis on the convective factor. This situation usually occurs during the summer when the nature, the time of appearance, and the physiognomy of the echo allow this kind of convection initiation to be confirmed.

The establishment of the diurnal evolution period has been defined in a time slot ranging from 08.00 to 20.00 UTC (10.00-22.00 local time), considering that practically all the convective diurnal evolution echoes take place within this range, a fact that the resulting hourly frequency graphs will confirm later.

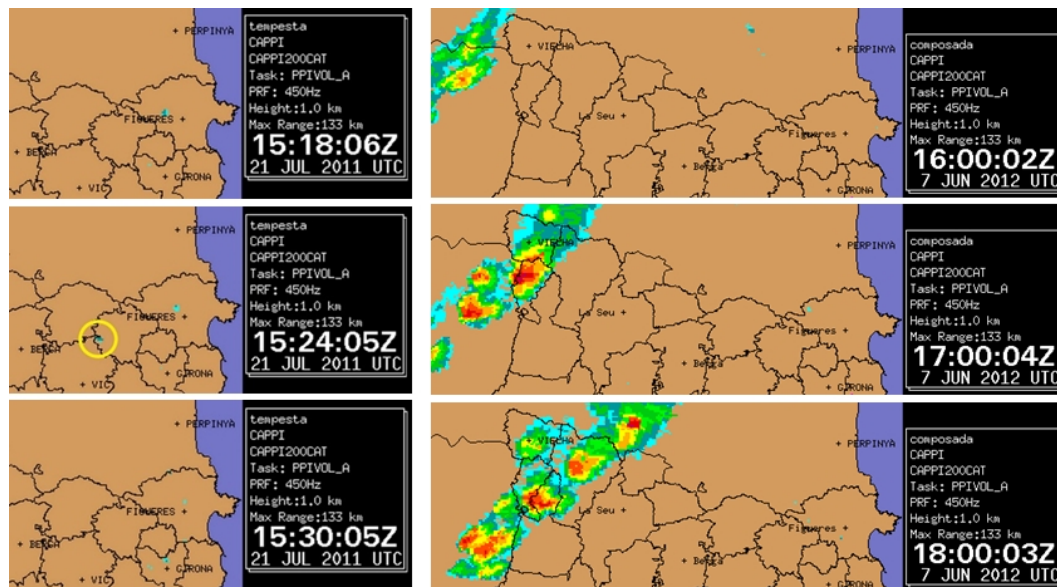


**Figure 6:** Examples of cases with anomalous echoes (transient echoes: on the left), or non-related echoes with diurnal evolution convection (migratory echoes; on the right). Both cases have been rejected in the analysis.

**Table 2:** Scheme of validating criteria for echoes used in the analysis.

Onset (8.00 - 20.00h)		Evolution	
Study area	Exterior area	Study area	Exterior area
echo15	x	echo15	echo15
		echo25+	echo25+
x	echo15	echo15	echo15
		echo25+	echo25+

Echo35 and Echo45	
Onset (8.00 - 20.00h)	Resolution
Study area	Valid
Study area migratory echoes day	Not valid
Exterior area	Not valid

### 3.2.2 Reflectivity Thresholds

The selection of the thresholds used for image classification was based on previously-defined criteria that take the relationship between convection intensity and reflectivity values into account.

The research team first designed an experiment which consisted of the automatic classification of echoes through complex algorithms applied to georeferenced GeoTIFF images. However, this option entails serious problems that are difficult to solve and may alter the validity of the results (see the presentation of the radar data in Section 2). In this respect, the main problems are those echoes that appear in the study area for the first time, although they originate in the outer area and therefore do not correspond to initial ‘in situ’ convection. The same is true for those ‘in situ’ echoes within migratory echoes on a non-convection day of diurnal evolution. The complexity of automatically discriminating and rejecting invalid echoes therefore means that the manual method is the best classification option. The

manual detection of these echoes is usually easy; either through the shape of the echo or by tracking different consecutive images. Other research work that involved convection onset and echo trajectories also applied manual classification methods (Hagen et al., 2011).

Several considerations need to be introduced before presenting the classification criteria:

- All echoes with a presence in solely a single image (or transient echoes), i.e. without continuity, have been discarded, as they are usually associated with abnormal interference or reflectivity (Fig. 6, left).
- Migratory echoes are defined as those generated outside the region of interest and that afterwards, have affected at least one of the 12 counties of the Catalan Pyrenees. The analysis only contemplates those that appear ‘in situ’ in the study area, and after outlier’s echoes have been discarded. The day with a clear predominance of these echoes, often associated with the passage of a front or trough in height, has been ruled out (Fig. 6, right).

From here, the criteria defined for each reflectivity threshold were as follows (Table 2):

- **15 dBZ (e15/echo15):** this reflectivity refers to the origin of the echoes. In this study this threshold refers to those echoes that originate within the study area and that subsequently reach - either in the study area or outside it -, at least, the reflectivity of 25 dBZ. If the above conditions are not met, the echo is discarded.
- **35 dBZ (e35/echo35):** regardless of where the initial echo (echo15) originated, these cells have reached 35 dBZ within the study area, so the e35 coming from

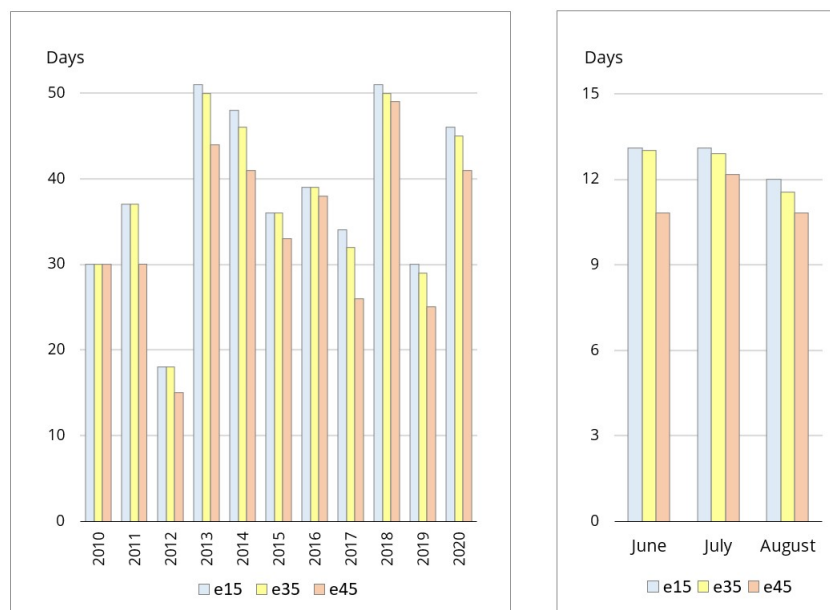


**Figure 7:** The distribution of the number of days with onset echoes of diurnal evolution convection in the Catalan Pyrenees (left) and the monthly distribution of the mean number of days with convection initiation of diurnal evolution (right).

**Table 3:** Statistical summary of the classification and analysis of days during the analysed period.

<b>Total number of days analysed</b>	<b>571</b>	<b>100%</b>
No data/imagery days	11	1.9%
Days without echoes between 08.00 and 20.00 UTC	35	6.1%
Discarded days: predominant transient or migratory echoes	73	12.8%
Doubtful days	27	4.7%
<b>Total non-classified days</b>	<b>146</b>	<b>25.6%</b>
<b>Total classified days</b>	<b>425</b>	<b>74.4%</b>

outside has been discarded. Furthermore, echoes from days when there is a general behaviour of migratory cells -those that originate from outside the study area- are discarded.

- **45 dBZ (e45/echo45):** same criteria as the e35 threshold.

Table 3 shows the total number of valid and discarded days, after applying the previous criteria and classifications to those echoes acceptable (with the reasons for exclusion).

## 4 Results

### 4.1 Temporal distribution

#### 4.1.1 Annual distribution

Fig. 7 (left) presents the annual distribution that corresponds to the summer period for the number of days when the onset of diurnal reflectivity echo threshold 15, 35 and 45 dBZ was confirmed. The average number of days

with echoes of 15 and 35 dBZ for the 2010-2020 period is around 38 days, while for those with echoes of 45 dBZ is approximately 34 days. This means that 35 and 45 dBZ echoes not also appear every day that 15 dBZ echoes occur. On the other hand, one of the main features shown in the graph is a remarkable interannual variability, with lows of 18 days for 15 and 35 dBZ, and 15 days for 45 dBZ, and highs of 51, 50 and 49 days respectively.

An almost regular distribution (Fig. 7, right) exists during these three months in the Catalan Pyrenees. This typical distribution occurs in each of the three categories of reflectivity, and ranges between 11 and 13 days on average. In overall terms, July points to a higher average while August has the lowest average number of recorded days, despite the small monthly differences.

#### 4.1.2 Hourly distribution

Given that this investigation focuses only on the echoes of onset of convection and not on the total number of convective cells, it is logical that hourly distribution shows a shift towards earlier hours. As Fig. 8 shows, the most frequent start of the first echo of 15 dBZ occurs during the 11.00-12.00 UTC time interval. It may also be stated from the histogram provided that the leading time slot for the start of this echo is from 10.00 to 13.00 UTC. The hourly frequency distribution shows regular increasing and decreasing dynamics, like that of a Gaussian bell with a bias to the right.

The appearance of the first echo of 35 dBZ, also reveals a higher frequency in the 11.00-12.00 UTC time interval, although it has a different dynamic when compared to echo 15 dBZ. In this case, the maximum frequency time slot

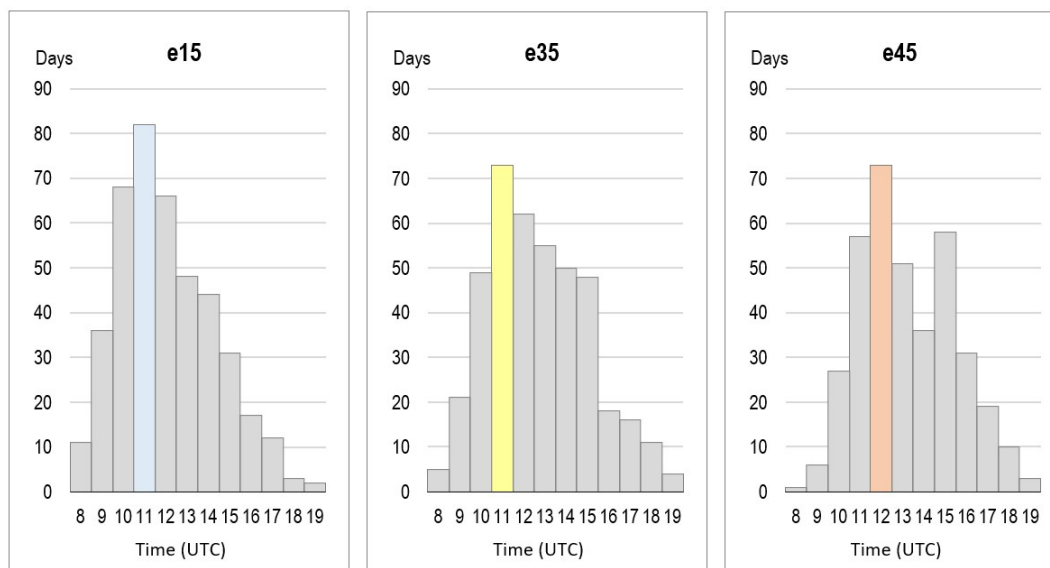


**Figure 8:** Hourly distribution of the first daily echo of diurnal evolution convection.

extends from 10.00 to 16.00 UTC (3 hours more than that of echo 15 dBZ). Furthermore, both the beginning and the end are more sudden in the latter case.

Finally, echo 45 dBZ reaches its maximum frequency at 12.00-13.00 UTC, one hour later than the other two echoes. In this case, a very specific dynamic is observed: after the maximum level occurs, the frequency should decrease with time, as with the echoes 15 and 35. However, a decrease in frequency begins with echo 45 dBZ, following the attainment of maximum levels, until 14.00-15.00 UTC and there is a sudden increase in the 15.00-16.00 UTC time interval, with this becoming the second maximum hourly frequency.

This behaviour of the three thresholds during the entire summer is not the same in the three summer months, which provide specific histograms (not shown). In broad, generic terms, the following lines summarize the main characteristics:

- As the summer progresses, a delay of the maximum frequency time in the three thresholds occurs (Table 4).
- The maximum values of the maximum frequency hourly interval occur in July for the three thresholds.
- The maximum frequency period intervals are more defined and homogeneous in August than in June and July.
- From 08.00 to 10.00 UTC (10.00-12.00 Local Time), the initial frequency of the 35 and 45 dBZ period intervals is either scarce or non-existent during July and August, although not in June, and it is very low in general, from 18.00 UTC throughout the summer and in all echoes.

**Table 4:** Time of maximum convection frequency by threshold.

Maximum frequency time slot			
Echos (dBZ)	June	July	August
e15	10-11	11-12	11-13
e35	10-11	11-12	13-14
e45	12-13	12-13	13-14

## 4.2 Spatial distribution

The initiation of summer diurnal evolution convection presents a seasonal, monthly and hourly time pattern that is well-defined in areas such as the Pyrenean region. In all events a spatial analysis is required that allows several hotspots to be found. These hotspot regions present a higher frequency of the first convective echoes that occur. In this case, the questions that arise are: do certain factors favour the occurrence of these first convective echoes? and which are these factors? In the case of non-clear hotspots, the distribution is random and heterogeneous, and affects all sectors in the same way.

### 4.2.1 Distribution in the Western and Eastern Sectors of the Catalan Pyrenees

The first part of the analysis presents the division of the Catalan Pyrenees between the Eastern and Western sectors, as defined in Section 2.1. The frequency distribution of the initial echoes between both sectors (Fig. 9) shows an evident inequality. On the one hand, the Eastern Pyrenean region has a higher frequency than its western counterpart. The absolute initial daily echoes of 15, 35, and 45 dBZ are located predominantly in the eastern areas of the Catalan Pyrenees. However, as the intensity of the reflectivity increases -referring to the initial echoes for the corresponding



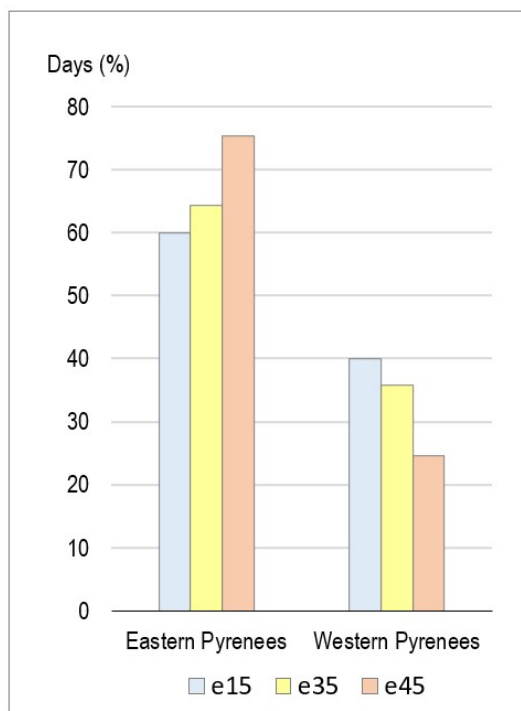


**Figure 9:** Frequency distribution (days) of convection initiation for the three thresholds (15, 35 and 45 dBZ) between the Eastern and Western Pyrenees.

threshold- the difference between the two sectors increases. As a result, echo15s appears firstly in the Eastern Sector during 60% of the days analysed, while in the Western Sector it appears in 40%. This percentage increases to almost 65% for echo35s in the east and drops to about 35% in the west.

Finally, echo45s occur for the first time in the Eastern Sector, in just over 75% of the total days in which these echoes appear, while not reaching a level of 25% when compared to the same days analysed in the Western sector.

#### 4.2.2 County-based Distribution

A more detailed analysis with respect to counties (the basis of the spatial classification of echoes) provides a better understanding of the spatial distribution and of differences in frequencies. The result of this analysis (Fig. 10) shows the marked and absolute predominance of the county of El Ripollès (Eastern Pyrenees) over all the other counties in all three thresholds. In this area, the daily initiation of diurnal evolution convection occurs most frequently than in the rest of the Catalan Pyrenees, accounting for approximately 1/3 of all recorded cases. In more detailed terms, these values range between 30% for echo15 and echo35 thresholds and 37% for echo45.

Since the surface area of the different counties is highly variable, the analysis and comparison of the frequency of the initial echoes in terms of county area must take this factor into account. As otherwise, the comparison would have a

bias that favours the larger regions, while underestimating the smaller ones. Calculating frequencies per unit area provides the figures for unified spatial density per surface area, that is, by dividing the number of cases by the county area (Fig. 10). Therefore, with respect to the echo15 threshold, the Alta Ribagorça acquires relative importance, and is the second-ranking county in terms of the daily frequency of daytime convection onset with about 15% of all cases. One could consider the existence of a second nucleus, one that is much less important than the first, and which is located in the Western Pyrenees. This second nucleus would also include the Val d'Aran, as this area registers the third-highest frequency.

The county of L'Alt Empordà should also be mentioned, this area lies very close to El Ripollès, however it has the lowest frequency values, in both echo15 and echo35 thresholds. Counties that are very near to each other have extreme maximum and minimum convection onset frequencies. In this sense, further research is needed to analyze the causes and factors that cause this profound disparity. In all events, a primary potential cause could result from the relief of L'Alt Empordà, with its much smaller orographic extension and more modest altitudes (reaching a maximum height of 1,451 m) while the altitudes in El Ripollès are close to 3,000 metres above sea level. As for the frequency of the echo45 threshold, L'Alt Empordà experiences a slight comparative increase, with higher values than L'Alt Urgell and El Pallars Jussà, as it is a county that receives echo cells of lower intensity that originate in El Ripollès. In our experience, we have seen how these storms intensify and reach the first echoes of 45 dBZ reflectivity during their trajectory when they begin to enter L'Alt Empordà.

#### 4.2.3 High Resolution Spatial Distribution

Finally, the last step of the analysis considered the maximum-scale spatial distribution of the frequency intensity of the first 15, 35 and 45 dBZ daily, non-migratory diurnal evolution echoes using the base source, in this case, the georeferenced raster radar images, that were created with a resolution of 1 km per pixel.

The convection onset (for the 15 dBZ threshold) occurs in the county of El Ripollès more than any other, as shown in the county-based analysis. The resulting map (Fig. 11, top), which shows the distribution and spatial frequency of the initial daily convection echoes, also reveals maximum density in this region. This level of analysis also allows us to specify the sectors of higher density and intensity within the area. In this respect the maximum concentrations and frequencies occur along the northern border, where higher relief is found. Furthermore a clear difference exists between the southern and northern half of the county.

As regards the rest of the Pyrenees, other secondary sectors may be noted, however it must be said that these are much smaller than El Ripollès, especially in terms of

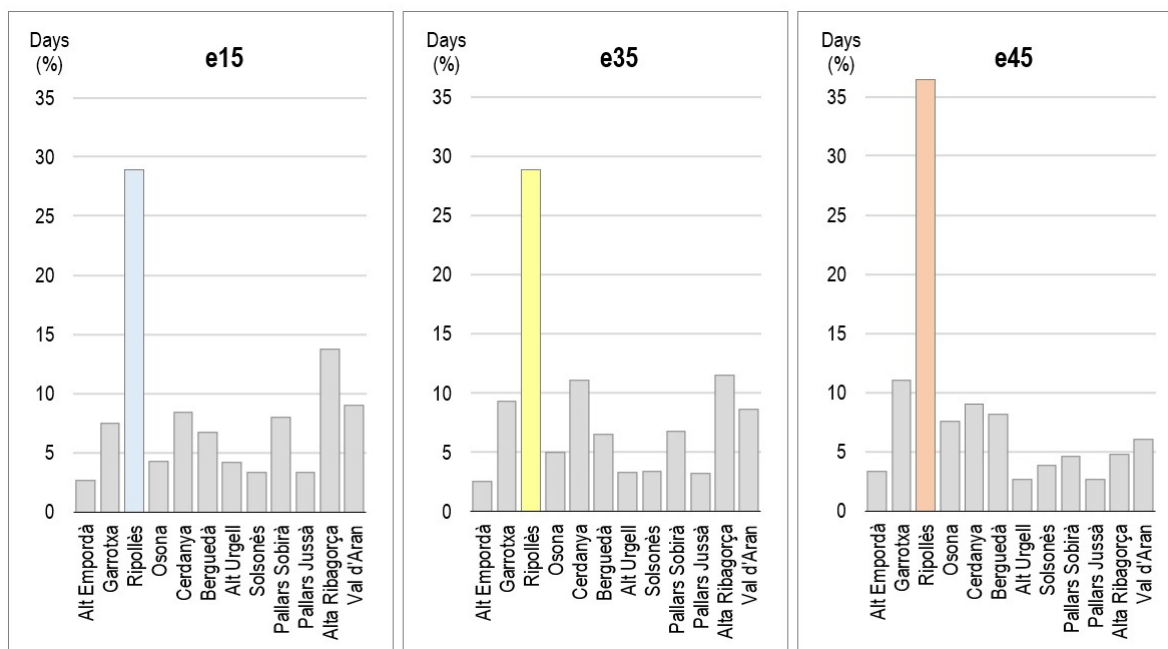


**Figure 10:** County-based distribution of the convection initiation for the different thresholds (15, 35 and 45 dBZ) per surface unit.

frequency: the northern half of L’Alta Ribagorça, and several small areas in the Val d’Aran, Pallars Sobirà and Pallars Jussà sectors, the northern extreme of the La Cerdanya and the north-eastern sections of El Solsonès and the north-central sector of El Berguedà.

The onset of echo35 (Fig. 11, centre) also occurs predominantly in El Ripollès, as indicated by county-based distribution. Maximum density affects the northern end of this county. Furthermore, considerable differences appear between the southern half, (with limited extension and frequency in terms of echo distribution), and the northern half, with maximum activity throughout the Pyrenees. In this case, unlike the initial convection of the echo15 threshold, only a second nucleus would be configured in an obvious way, especially in terms of extension, although it would be much less meaningful than that of El Ripollès. This nucleus would be configured by the extreme northeastern sector of El Solsonès with the north-central sector of the Berguedà, and it would correspond to a relevant orography. The rest of the echo35 starting areas have a very random distribution and small nuclei throughout the Pyrenees.

Finally, the spatial distribution and frequency of daily onset of echo45 (Fig. 11, bottom) are both smaller than for the lower reflectivity intensities, this being a frequent feature as reflectivity increases. Once again, the northern extreme of El Ripollès is the most important in the whole Pyrenees and, in general, a large part of the northern half of the county is quite remarkable. This sector, therefore, is confirmed by the three thresholds that have been analysed as an exclusive hotspot in terms of the maximum frequency of the daytime convection initiation throughout the Pyrenees.

With respect to the rest of the territory, some localised nests of small extension and intensity exist. The most

important of these corresponds to the northern end of La Val d’Aran, as a singularity of the Western Pyrenees. In terms of the Eastern Pyrenees, the sector that in the other two echo thresholds (15 and 35 dBZ) stood out, is now distorted, i.e. the north-eastern end of El Solsonès and north-central Berguedà.

## 5 Discussion

The period of analysis (which includes the three summer months -June, July and August-) corresponds to the warmest period of the year. This period includes the maximum convective activity, as can also be seen with the frequency of stormy days (Núñez et al., 2018). The total number of convective cells also has similar characteristics and analogous behaviour to the number of days with echoes of diurnal evolution being recorded, as shown by other studies (Burcea et al., 2019) that are based on radar images.

Regarding the daily cycle of convection, the cells of diurnal evolution generally show a maximum frequency during the afternoon, which coincides with several studies -despite variations in time, duration and intensity of convection-: between 12.00 and 14.00 UTC (Sangiorgeo and Barindelli, 2020), around 15.00 UTC (Kaltenboeck and Steinheimer, 2015), between 12.00 and 16.00 UTC (Burcea et al., 2019).

Finally, the problem in obtaining reliable results of the spatial distribution of high-resolution echoes lies fundamentally in the natural behaviour of convection. As stated above, the application of automatic algorithms does not allow its detection and classification. Furthermore, the complexity of convection classification may be solved, without much difficulty, through manual analysis. However, those problems

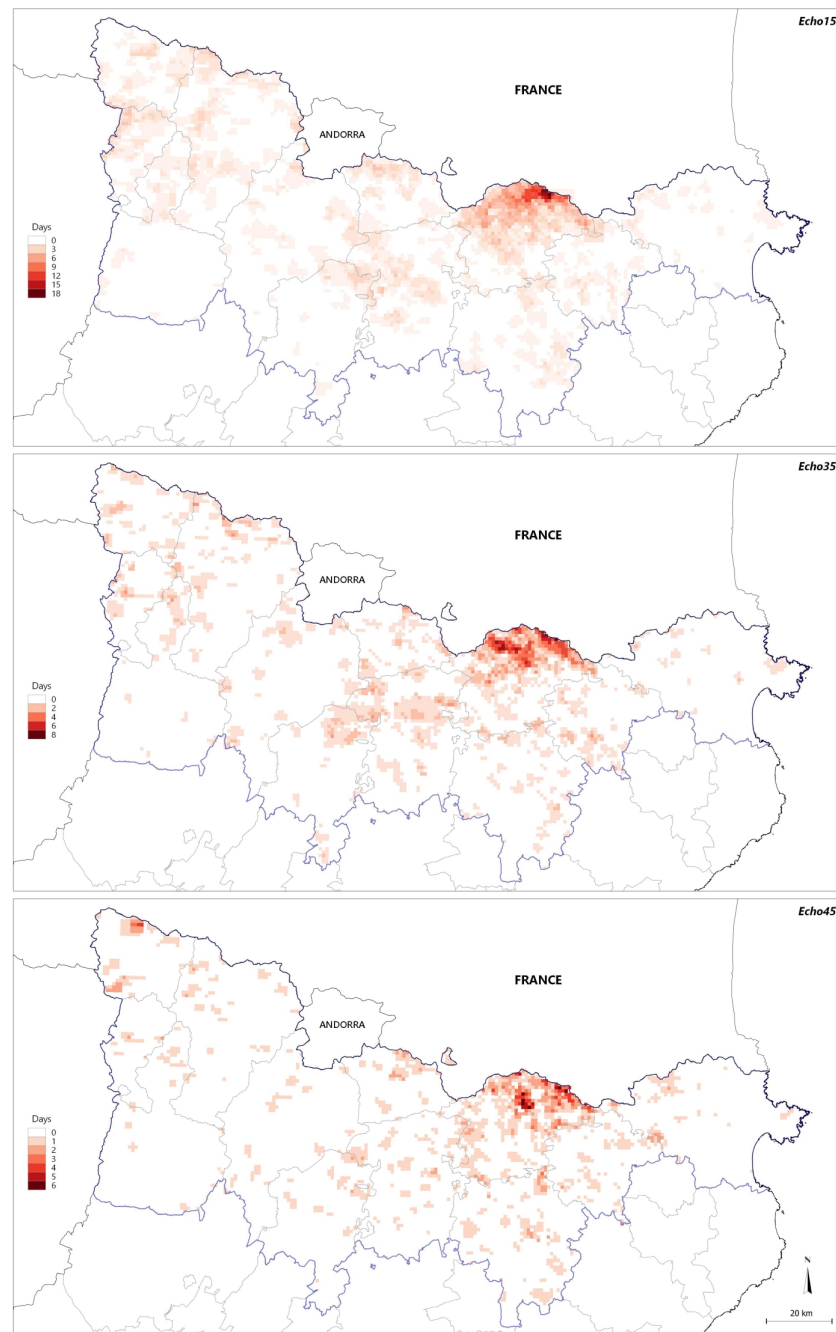


**Figure 11:** Spatial distribution and frequency of the summer convection initiation for echo15 dBZ (top), echo35 dBZ (centre) and echo45 dBZ (bottom) thresholds, for the 2010-2020 period.

derived from elements external to convection, such as those of the radar itself, in which, for example, interference may occur -in this case this is easily perceptible (Fig. 12, left). When carrying out geostatistical procedures these anomalies are reflected in the analysis and distort the results. In this study interference has been present on one of the four radars for two summers, and so it has been necessary to differentiate the interference signal from that of valid convective echoes through daily corrections and an explicit algorithm application has been used for this purpose. The correct

images are finally obtained once the anomalous reflectivities have been removed (Fig. 12, right). It is worth mentioning that, fortunately, these types of interference very rarely generate reflectivities that exceed 25 dBZ -as has occurred with this research work-, and as such only the first level of echoes (echo15) were affected and required correction.

It is important to finish this section by saying that the area identified with the maximum activity, the northern area of El Ripollès, coincides with that found in the analysis of Conde Iglesias (2021), although the data used is different

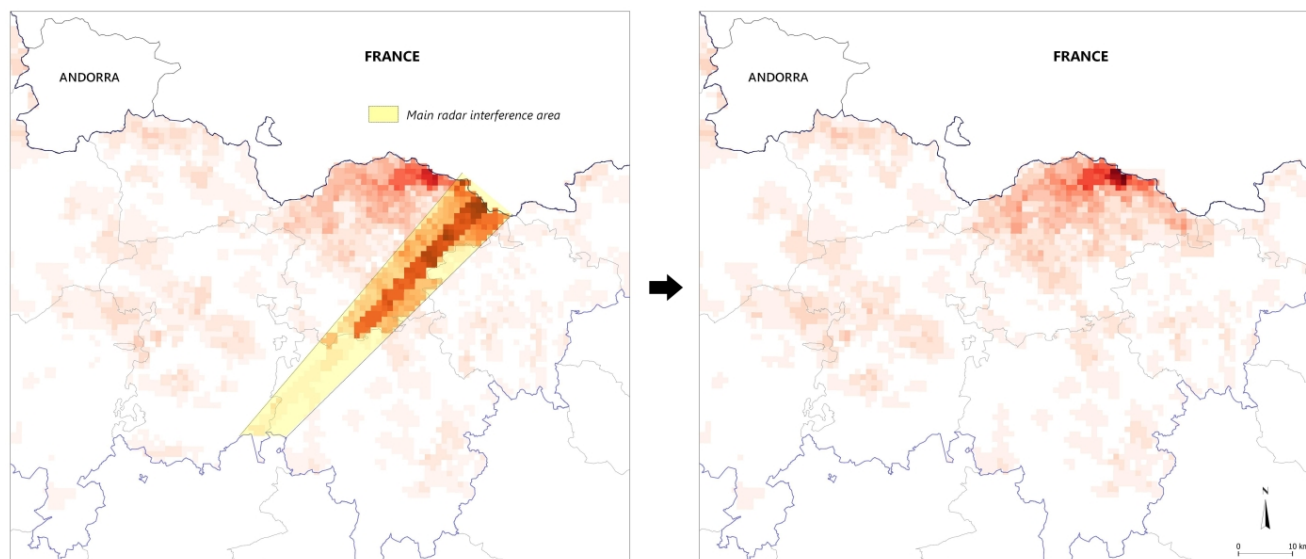


**Figure 12:** Example of the recurrent electromagnetic interference affecting the radar imagery (left) and after correction (right).

(lightning detection versus radar) and the analysed region in that research work corresponded to Catalonia as a whole.

## 6 Conclusions

The spatial and temporal analysis of early summer diurnal evolution convection reveals both irregularity in its spatial distribution along the Catalan Pyrenees and in general, a considerable correspondence between the daily cycle of the hourly frequency of the phenomenon and the daily thermal regime.

Convection onset in the Pyrenees occurs predominantly between 10.00 and 13.00 UTC, a few hours before the maximum daily temperature occurs. The later temperature increase contributes to the evolution of the cell. As the summer progresses, the time slot for the maximum initiation frequency of the three types of convection -weak, moderate and intense- occurs later in the day.

The spatial disparity observed in the frequency of onset of convection is substantial for the three types of reflectivity intensity. The county of El Ripollès stands out as a nest of initial convection, especially in its northern half. In general, there is a good correspondence between the starting convection frequencies (echo15 dBZ) and the relief in the whole region of interest. The orographic factor is therefore one of the main aspects that favours convection onset.

This work has focused on the Catalan Pyrenees however, given the results, it would be interesting to expand the study area beyond the border, especially in its eastern sector, to find out if the French Pyrenees behave in the same way, and to discover the possible existence of other nests of initial convection.

Also, a search for the initialisation of all the convective echoes -not only the first ones- would provide us with almost complete knowledge of the behaviour and dynamics of the

diurnal evolution convection and would allow us to define those areas of higher frequency.

Finally, the possibility of extending the analysis period to the months of May and September could be considered, as both these periods still show noteworthy convective activity when studies of storm climatology in the Pyrenees are observed.

## Acknowledgments

The authors would like to thank to the Meteorological Service of Catalonia for the data provided.

## References

- Abancó, C., Hürlimann, M., Moya, J., and Berenguer, M., 2016: *Critical rainfall conditions for the initiation of torrential flows. Results from the Rebaixader catchment (Central Pyrenees)*, J. Hydrol., **541**, 218–229.
- Altube, P., Bech, J., Argemí, O., and Rigo, T., 2015: *Quality control of antenna alignment and receiver calibration using the sun: Adaptation to midrange weather radar observations at low elevation angles*, J. Atmos. Ocean. Technol., **32**, 927–942.
- Aoshima, F., Behrendt, A., Bauer, H.-S., and Wulfmeyer, V., 2008: *Statistics of convection initiation by use of Meteosat rapid scan data during the Convective and Orographically-induced Precipitation Study (COPS)*, Meteorol. Z., **17**, 921.
- Aznárez-Balta, M., Llasat, M. C., Llasat-Botija, M., Cortès, M., Gilabert, J., and Quintana-Seguí, P., 2020: *Floods in the Pyrenees region: the PIRAGUA-FLOOD geodatabase*, in: EGU General Assembly Conference Abstracts, p. 5462.
- Bai, L., Chen, G., and Huang, L., 2020: *Image processing of radar mosaics for the climatology of convection initiation in South China*, J. Appl. Meteorol. Climatol., **59**, 65–81.
- Burcea, S., Cică, R., and Bojariu, R., 2019: *Radar-derived convective storms' climatology for the Prut River basin: 2003–2017*, Nat. Hazards Earth Syst. Sci., **19**, 1305–1318.



- Conde Iglesias, A.: *Identificació dels nius de tempestes a partir d'un model meteorològic*, treball final de Màster de Meteorologia, Facultat de Física, Universitat de Barcelona, 2021.
- Corripio, J. G. and López-Moreno, J. I., 2017: *Analysis and predictability of the hydrological response of mountain catchments to heavy rain on snow events: a case study in the Spanish Pyrenees*, *Hydrology*, **4**, 20.
- del Moral, A., del Carmen Llasat, M., and Rigo, T., 2017: *Identification of anomalous motion of thunderstorms using daily rainfall fields*, *Atmos. Res.*, **185**, 92–100.
- del Moral, A., Rigo, T., and Llasat, M. C., 2018: *A radar-based centroid tracking algorithm for severe weather surveillance: Identifying split/merge processes in convective systems*, *Atmos. Res.*, **213**, 110–120.
- Farnell, C. and Rigo, T., 2020: *The Lightning Jump, the 2018 “Picking up Hailstones” Campaign and a Climatological Analysis for Catalonia for the 2006–2018 Period*, *Tethys*, **17**, 10–20.
- Frye, J. D. and Mote, T. L., 2010: *Convection initiation along soil moisture boundaries in the southern Great Plains*, *Mon. Weather Rev.*, **138**, 1140–1151.
- Goudenhoofd, E. and Delobbe, L., 2013: *Statistical characteristics of convective storms in Belgium derived from volumetric weather radar observations*, *J. Appl. Meteorol. Climatol.*, **52**, 918–934.
- Gray, J., 2008: *Quantum GIS: the open-source geographic information system*, *Linux Journal*, **2008**, 8.
- Hagen, M., Van Baelen, J., and Richard, E., 2011: *Influence of the wind profile on the initiation of convection in mountainous terrain*, *QJRM*, **137**, 224–235.
- Huang, Y., Meng, Z., Li, J., Li, W., Bai, L., Zhang, M., and Wang, X., 2017: *Distribution and variability of satellite-derived signals of isolated convection initiation events over central Eastern China*, *J. Geophys. Res.*, **122**, 11–357.
- Jansa, A., Homar, V., Romero, R., Alonso, S., Guijarro, J., and Ramis, C., 2017: *Extension of summer climatic conditions into spring in the Western Mediterranean area*, *Int. J. Climatol.*, **37**, 1938–1950.
- Kaltenboeck, R. and Steinheimer, M., 2015: *Radar-based severe storm climatology for Austrian complex orography related to vertical wind shear and atmospheric instability*, *Atmos. Res.*, **158**, 216–230.
- Llasat, M. C. and Puigcerver, M., 1994: *Meteorological factors associated with floods in the north-eastern part of the Iberian Peninsula*, *Nat. Hazards*, **9**, 81–93.
- Mecikalski, J. R., Bedka, K. M., Paech, S. J., and Litten, L. A., 2008: *A statistical evaluation of GOES cloud-top properties for nowcasting convective initiation*, *Mon. Weather Rev.*, **136**, 4899–4914.
- Meteorological Service of Catalonia: *Atles climàtic de Catalunya 1961–1990*, Tech. rep., Meteorological Service of Catalonia, 2008.
- Núñez, J. A., Mora, M. A., and Riesco, J.: *Climatología básica de tormentas en España*, sexto Simposio Nacional de Predicción Memorial Antonio Mestre, 247–258. AEMET. Madrid, 2018.
- Pascual, R., Callado, A., and Berenguer, M., 2004: *Convective storm initiation in central Catalonia*, *Proc. of ERAD04*, pp. 464–468.
- Pineda, N., Soler, X., and Vilaclara, E., 2011: *Aproximació a la climatologia de llamps a Catalunya*, Nota d'estudi del Servei Meteorològic de Catalunya, Generalitat de Catalunya B-7024-2011, **73**.
- Pino, D., Ruiz-Bellet, J. L., Balasch, J. C., Romero-León, L., Tuset, J., Barriendos, M., Mazon, J., and Castellort, X., 2016: *Meteorological and hydrological analysis of major floods in NE Iberian Peninsula*, *J. Hydrol.*, **541**, 63–89.
- R Core Team, 2013: *R: A language and environment for statistical computing*.
- Rigo, T. and Llasat, M., 2004: *A methodology for the classification of convective structures using meteorological radar: Application to heavy rainfall events on the Mediterranean coast of the Iberian Peninsula*, *Nat. Hazards Earth Syst. Sci.*, **4**, 59–68.
- Rigo, T. and Llasat, M. C., 2016: *Forecasting hailfall using parameters for convective cells identified by radar*, *Atmos. Res.*, **169**, 366–376.
- Rigo, T., Pineda, N., and Bech, J., 2010: *Analysis of warm season thunderstorms using an object-oriented tracking method based on radar and total lightning data*, *Nat. Hazards Earth Syst. Sci.*, **10**, 1881–1893.
- Rigo, T., Llasat, M. C., and Esbrí, L., 2021: *The Results of Applying Different Methodologies to 10 Years of Quantitative Precipitation Estimation in Catalonia Using Weather Radar*, *Geomatics*, **1**, 347–368.
- Riosalido, R., Ferraz, J., Alvarez, E., Cansado, A., Martín, F., Elízaga, F., Camacho, J., and Martín, A., 1997: *A flash flood event in the Spanish Pyrenees: the Biescas case*. INM, in: WMO International Symposium on cyclones and hazardous weather in the Mediterranean, Palma de Mallorca, pp. 151–158.
- Sangiorgio, M. and Barindelli, S., 2020: *Spatio-temporal analysis of intense convective storms tracks in a densely urbanized Italian basin*, *ISPRS Int. J. Geo-Information*, **9**, 183.
- Utsav, B., Deshpande, S. M., Das, S. K., and Pandithurai, G., 2017: *Statistical characteristics of convective clouds over the Western Ghats derived from weather radar observations*, *J. Geophys. Res.*, **122**, 10–050.
- Weckwerth, T. M. and Parsons, D. B., 2006: *A review of convection initiation and motivation for IHOP\_2002*, *Mon. Weather Rev.*, **134**, 5–22.
- Wilson, J. W., Moore, J. A., Foote, G. B., Martner, B., Rodi, A. R., Uttal, T., and Wilczak, J. M., 1988: *Convection initiation and downburst experiment (CINDE)*, *Bull. Am. Meteorol. Soc.*, **69**, 1328–1347.